ACS EARTH AND SPACE CHEMISTRY
http://pubs.acs.org/journal/aesccq
Article

# Thermal Evolutions and Resulting Microstructural Changes in Kerogen-Rich Marcellus Shale

Cody B. Cockreham, Xianghui Zhang, Miu Lun Lau, Min Long, Xiaofeng Guo, Hongwu Xu,* and Di Wu*

Cite This: *ACS Earth Space Chem.* 2020, 4, 2461−2469
Read Online

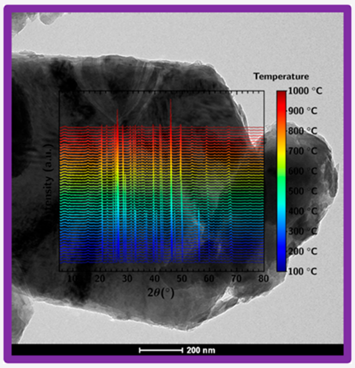

**ABSTRACT:** Shale rock is a complex geochemical system, which contains inorganic minerals and organic matter (e.g., kerogen), of which the latter possesses porous, high-molecular-weight carbon structures. The pores within organic matter hold the majority of recoverable unconventional oil and natural gas. The organic matter also provides a possible source of hydrocarbon fuel upon pyrolysis. To promote engineering developments in hydrocarbon recovery using heating methods, it is essential to have a fundamental understanding of the nature of the thermal behavior of shale. Consequently, we have investigated the thermal evolution of a shale sample from the Marcellus Formation, Pennsylvania, using a multi-faceted materials science approach, including *in situ* X-ray diffraction, *in situ* diffuse reflectance spectroscopy, thermogravimetric analysis coupled with differential scanning calorimetry and mass spectrometry, and transmission electron microscopy. Our aim was to link the naturally heterogeneous and complex chemistry of the shale with its mineralogy and thermal stability up to 900 °C. The thermally induced decomposition of organic and inorganic phases resulted in systematic changes in the shale characteristics. More specifically, kerogen underwent complex decomposition reactions between 200 and 600 °C, depending upon the heating rate and atmosphere (oxidative or inert); pyrite decomposed from 300 to 400 °C; and above 600 °C, inorganic minerals, such as carbonate and clay, broke down. These decompositions created microscopic cracks and left empty pores within the rock. Our results provide insight into the pyrolysis process of shale for hydrocarbon recovery.

**KEYWORDS:** *shale, guest−host interactions, thermal analysis, calorimetry, in situ X-ray diffraction, kerogen*

## ■ INTRODUCTION

Shale rock is at the forefront of fossil energy production, holding large storages of unconventional oil and gas, and thus is also at the center of environmental considerations, especially in terms of groundwater pollution.[1−4] Shale is a fine-grained sedimentary rock typically containing a mixture of clays (illite and smectite), quartz, feldspar, carbonates (calcite and dolomite), and pyrite, but most importantly, it also contains kerogen, a complex organic matter of highly linked heavy-molecular-weight carbons, including aromatic and aliphatic carbons.[5−7] Within a wide distribution of inorganic or organic macro-, meso-, and micropores of shale hold valuable oil and gas products. Current research focuses on industrially relevant issues associated with extraction of oil and gas, including measuring the pore structure of shale and modeling the behavior of its confined hydrocarbon fluids.[8−15]

Previous efforts have investigated microstructural characteristics of shale after thermal treatments and their relation to mineral compositions. Specifically, Liu et al. linked the thermal evolution of structural (crystallographic) to microstructural (pores and surface areas) changes using experimental techniques, including scanning electron microscopy, adsorption analysis, and X-ray-based techniques: ultrasmall, small, and wide-angle X-ray scattering.[16] A number of studies characterized the thermal evolution of oil and gas products and decomposition mechanisms of kerogen during pyrolysis.[17−22] In addition, the thermal behavior and phase transformations of inorganic constituents of shale, such as quartz, feldspars, clays, carbonates, and pyrite, have been well-studied.[23−27] Nevertheless, there are still knowledge gaps in the thermal evolution, especially of kerogen, that require further studies. With the focus on the fundamental materials science aspects of shale (which is essentially a hybrid composite material) upon thermal treatment, we aim to link its thermal evolutions with its chemistry, mineralogy, and microstructure. The goal is to complement the previous application-focused studies by investigating fundamental aspects of shale thermal behavior.

**Special Issue:** Materials of the Universe: The Final Chemical Frontier

**Received:** August 26, 2020
**Revised:** November 10, 2020
**Accepted:** November 13, 2020
**Published:** November 30, 2020

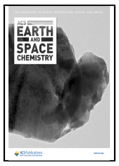

https://dx.doi.org/10.1021/acsearthspacechem.0c00234

The characteristics of shale components as well as how they are assembled (microstructure) essentially determine the products and mechanisms of thermal decomposition. Such characteristics include type of organic matter, inorganic mineral species, porosity, permeability, etc. Therefore, with the application of a materials science perspective, we can gain valuable information on shale thermal evolutions. The shale sample studied, which has a high total carbon content, was retrieved from the Marcellus basin in Pennsylvania, a major unconventional shale gas formation in the United States. To probe the thermal behavior of Marcellus shale as a function of the temperature under different gas atmospheres, we employed several *in situ* high-temperature techniques, including *in situ* powder X-ray diffraction (XRD), *in situ* diffuse reflectance infrared Fourier transform spectroscopy (DRIFTS), and integrated thermogravimetry, differential scanning calorimetry, and mass spectrometry (TG−DSC−MS). We also used *ex situ* transmission electron microscopy (TEM) to characterize the samples before and after heat treatment. The advantages of applying our methodology are twofold: first, it provides a detailed *in situ* account of thermal behavior, which may be directly related to applications such as pyrolysis for oil and gas recovery, and second, it allows us to peak into the complexities of our shale from a post-mortem forensic perspective by piecing together implications of its high-temperature behavior. Simply put, this study provides fundamental insights into the thermal behavior of Marcellus shale, which have important implications for hydrocarbon recovery from unconventional reservoirs.

## ■ EXPERIMENTAL METHODS

**Source Materials.** The shale was retrieved from the Marcellus formation in Pennsylvania, U.S.A. A Marcellus shale core taken from a depth of 7544.15−7546.80 ft was provided by the Marcellus Shale Energy and Environmental Laboratory (MSEEL), a multi-disciplinary and multi-institutional effort focused on improving unconventional resource recovery. The Marcellus formation is the largest natural gas field in the United States, and Marcellus shale at the MSEEL site primarily consists of siliciclastic mudstones with interbedded carbonates.[28] The powder sample characterized in this work was from a portion of the Marcellus shale core.

**Compositional Analysis.** Inductively coupled plasma optical emission spectrometry (ICP−OES) was used to analyze the cationic composition following United States Environmental Protection Agency (U.S. EPA) Method 200.7 with a PerkinElmer Optima 2100 DV instrument. The standards used for calibration were purchased from SPEX Certiprep, Inc. To prepare the sample for ICP−OES, approximately 35 mg of powder was added to a Teflon digestion vessel. The solvents (2 mL of hydrogen peroxide, 1 mL of hydrofluoric acid, and 5 mL of nitric acid) were added to the vessel and allowed to react in the unopened vessel for 30 min. The vessel was then sealed and heated in a Titan MPS microwave system for two cycles (70 min per cycle) with a maximum operating temperature of 220 °C. After the mixture was cooled, 10 mL of 4% boric acid was added to each vessel to neutralize HF. Loss on ignition (LOI) analysis was performed by weighing a ∼1.0 g aliquot in a quartz crucible. It was treated in air at 1000 °C in a Thermolyne muffle furnace, held for 30 min, and reweighed upon cooling. The LOI is the percentage of mass loss from the heat treatment process.

**Thermal Analysis.** Thermal analyses using TG−DSC−MS were carried out on a Netzsch Instrument STA 449 F5 Jupiter coupled to a QMS 403 D Aëolos quadrupole mass spectrometer. For analysis in an inert environment, about 20 mg of powder sample was analyzed in an alumina crucible from 40 to 1000 °C at 10 °C/min under 50 mL/min nitrogen flow. For analysis in an oxidizing environment, about 20 mg of powder sample was analyzed in an alumina crucible from 40 to 1000 °C at 5 °C/min under 50 mL/min air flow. During multiple step thermal analysis, about 20 mg of powder sample was placed in an alumina crucible analyzed in a multi-step thermal program, including atmosphere change at 600 °C, specifically, (i) dynamic heating from 40 to 600 °C at 5 °C/min under 50 mL/min nitrogen flow, (ii) isothermal heating at 600 °C for 30 min under 50 mL/min nitrogen flow, (iii) isothermal heating at 600 °C for 30 min under 50 mL/min air flow, and (iv) dynamic heating from 600 to 1000 °C at 5 °C/min under 50 mL/min air flow. Evolved gases of TG−DSC experiments were identified simultaneously by the coupled MS. Each set of data was analyzed using the Proteus and Dispsav software packages. All MS, derivative thermogravimetry (DTG), and derivative differential scanning calorimetry (DDSC) curves were plotted using Origin. We have applied similar integrated thermal analysis methods on solid-state materials with microporosity and interlayer spaces in several ealier studies.[29−32]

**Electron Microscopy.** We examined the sample morphology using TEM (FEI Tecnai T20 with a $LaB_6$ cathode at 200 kV) in the Franceschi Microscopy and Imaging Center at Washington State University. ImageJ (National Institutes of Health) was employed for micrograph analysis.[33] The TEM specimens were prepared by dispersing a small amount of sample powder in ethanol using ultrasonication. Subsequently, the suspension was dried on 200-mesh carbon-coated nickel grids. Samples investigated were treated at the target temperature isothermally for 3 h using a tube furnace in an argon atmosphere.

***Ex Situ* and *In Situ* DRIFTS.** The *in situ* DRIFTS measurements were carried out in a high-temperature cell (Spectra-Tech) equipped with ZnSe windows. The spectra were collected from 30 to 600 °C under 50 mL/min helium flow with a hold time of 2 min at each temperature step. The sample powder was mixed with KBr at a ratio of 1:10 (shale/KBr) and placed in a ceramic crucible, and KBr was also used to collect background spectra. *Ex situ* DRIFTS data were recorded at 30 °C after isothermal treatment at the desired temperatures for 3 h using a tube furnace in an argon atmosphere.

***In Situ* XRD.** The structural evolution as the temperature increases from room temperature to 1000 °C was monitored by *in situ* powder XRD. The data were obtained using a Rigaku Smartlab X-ray diffractometer with Cu K$\alpha$ radiation ($\lambda$ = 1.5406 Å) coupled with the Rigaku HT1500 heating stage with a platinum strip crucible operated at a scan rate of 4°/min in the $2\theta$ range of 5−80° with a heating rate of 10 °C/min under 40 mL/min of helium with a hold time of 5 min prior to each scan. To create the three-dimensional (3D) XRD plots of intensity as a function of $2\theta$ and temperature, the Python tool of "Plotly" was employed to extract the data points and create 3D surface maps accordingly. To highlight changes in representative peaks in selected $2\theta$ ranges, an optimized color bar for each was created to better visualize details. To determine representative peaks for inorganic minerals in our

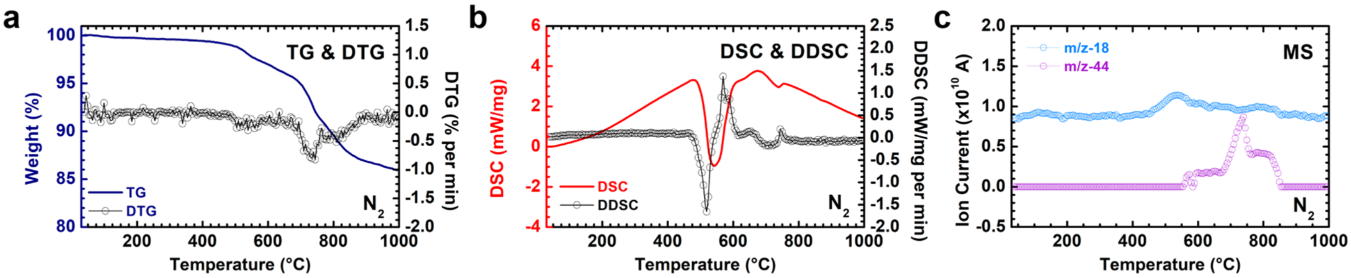

**Figure 1.** (a) TG and DTG, (b) DSC and DDSC, and (c) MS data of $m/z$ = 18 and 44, in nitrogen at 10 °C/min of Marcellus shale.

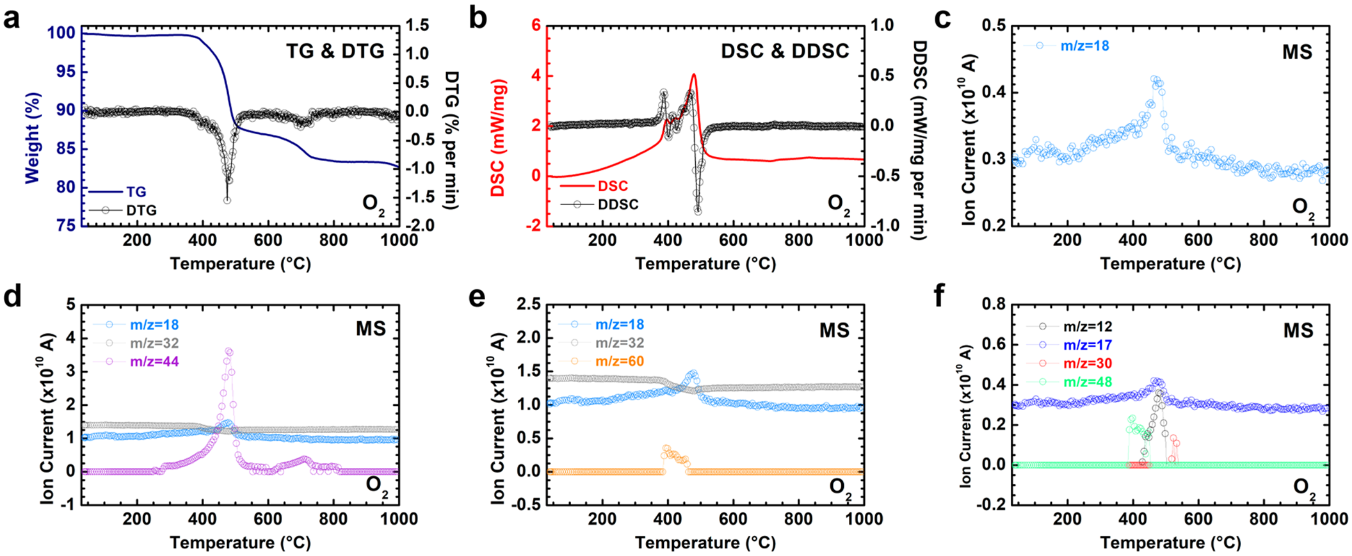

**Figure 2.** (a) TG−DTG, (b) DSC−DDSC, and MS curves (c) $m/z$ = 18 ($H_2O$), (d) $m/z$ = 18 ($H_2O$), $m/z$ = 32 ($O_2$), and $m/z$ = 44 ($CO_2$), (e) $m/z$ = 18 ($H_2O$), $m/z$ = 32 ($O_2$), and $m/z$ = 60 ($SO_2$), and (f) $m/z$ = 12 (C), $m/z$ = 17 (OH), $m/z$ = 30 (NO), and $m/z$ = 48 (SO), in oxygen at 5 °C/min of Marcellus shale.

XRD patterns, the American Mineralogist Crystal Structure Database (AMCSD) was used as follows: quartz, AMCSD 0000789; pyrite, AMCSD 0000006; illite, AMCSD 0005015; calcite, AMCSD 0000098; and orthoclase, AMCSD 0000313.

## ■ RESULTS AND DISCUSSION

**Phase and Compositional Analyses.** To investigate the composition of our shale sample, we performed XRD for crystalline phases, ICP−OES for a relative composition of cationic elements (see Table S1 of the Supporting Information), and LOI to estimate the total organics and other combustible species. The room-temperature XRD patterns indicate a mixture of quartz, feldspar, pyrite, illite clay, and calcite phases. The ICP−OES analysis shows predominately Si and Al with significant amounts (>1%) of Na, Mg, K, Ca, and Fe. The LOI is 15.51 wt % and includes contributions from all species that were removed during heat treatment in air at 1000 °C, including water and/or hydroxyl groups from clays, organic carbons (kerogen, etc.), inorganic carbon (carbonates), sulfur (pyrite), etc. Further, the thermal analyses using integrated TG−DSC−MS provide a more detailed composition of species, which were removed during LOI.

**Thermal Analysis in an Inert Atmosphere.** As the first step of investigating the thermal behavior of shale, we apply thermal analysis techniques using integrated TG−DSC−MS. The data of thermal analysis under $N_2$, mimicking pyrolysis conditions are presented in panels a−c of Figure 1. Overall, three general stages of thermal decomposition are evidenced. In stage I (−0.70 wt %), dehydration sees the loss of weakly and tightly (pore/layer confined) adsorbed water and dehydroxylation of clays up to 450 °C. Evidenced by the MS $m/z$ = 18 peaks in Figure 1c, weakly adsorbed water evolves, peak at ∼114 °C, and more tightly bound water is removed from interlayers of clays and pores, peaks at ∼214 and ∼334 °C, and clay dehydroxylates, peak at about 414 °C. Stage II (−7.48 wt %) sees the decomposition of kerogen into light and heavy organics, inorganic gases, and coke from 450 to 750 °C, shown by the DTG and DSC (endothermic) peaks at 534 and 524 °C, respectively.[19−21,34] The DSC peak occurring before the DTG peak points to mass transport limitations as a result of the inaccessible closed and open pores within rock and kerogen networks. Water and $CO_2$ are evolved from the decomposition of carbonates, suggested by $m/z$ = 18 peaks at 534 and 654 °C and $m/z$ = 44 peaks at 569 and 654 °C.[35−37] Further, during stage II, pyrite ($FeS_2$) decomposes to pyrrhotite ($Fe_{1-x}S$) completely by 600 °C and finally to troilite (FeS) at 800 °C.[38] Finally, stage III (−5.88 wt %), 750−1000 °C, contains the decarbonation of carbonate phases, including hydrated carbonate phases; see the DTG and DSC (endothermic) peaks at ∼727 and ∼737 °C, respectively, as well as the $m/z$ = 18 peak at 784 °C and $m/z$ = 44 peaks at ∼734 and ∼784 °C.[39] The higher temperatures of carbonate decomposition are likely due to mass transfer limitations within the tight void space of the shale structure. The total weight loss observed up to 1000 °C is 14.06 wt %, which correlates well with the LOI analysis.

**Thermal Analysis under Oxidative Environments.** To further our understanding of the thermal evolution of the Marcellus shale, we conducted measurements in air. Thermal analyses in this oxidative condition, TG−DTG, DSC−DDSC, and $m/z$ = 18, 32, 44, and 64 curves from 40 to 1000 °C, are shown in panels a, b, c, d, e, and f of Figure 2, respectively. Stage I (−0.15 wt %), as in the inert environment, suggests the loss of weakly and tightly adsorbed water up to ∼285 °C, evidenced by the MS $m/z$ = 18 peak of 103 and 190 °C, respectively. Stage II is complex and contains multiple events (−12.95 wt %). First, the combustion of pyrite ($FeS_2$) to Fe oxide species hematite, $\alpha$-$Fe_2O_3$, or magnetite, $Fe_3O_4$, and SO/$SO_2$ proceeds, shown by the DTG, DSC (exothermic), and MS $m/z$ = 64 peaks at 399, 396, and 399 °C, respectively.[40] Subsequently, the dehydroxylation of clay species ensues, shown by the small, broad DTG and DDSC (endothermic, hidden in the DSC by the strongly exothermic combustion reactions) at about 422 and 427 °C, respectively. Lastly, the combustion of kerogen and decomposition of carbonates, beginning at ∼285 °C, into $CO_2$ and water occurs, suggested by the DTG and DSC (exothermic) peaks both at 479 °C as well as MS $m/z$ = 18, 32, and 44 peaks at 474, 479, and 479 °C, respectively. As a result of the fast combustion of organic kerogen species and the high mobility of $CO_2$, there appears to be no large mass transport limitations. Stage III (−3.50 wt %) sees the decomposition of multiple carbonate species, evidenced by DTG, DSC (endothermic, shown in the zoomed-in view of Figure S1 of the Supporting Information), and $m/z$ = 44 MS peaks at 710, 711, and 709 °C. The total weight loss observed up to 1000 °C is 16.60 wt %, which correlates well with the LOI analysis. Showing slightly higher mass loss may be due to lower mass transport limitations, ∼20 mg of powder versus 1 g of aliquot. The mass loss is higher than in the pyrolysis ($N_2$) environment, expected to be due to coking of kerogen and incomplete desulfurization of pyrite, as pyrite decomposes to pyrrhotite and then troilite (FeS).[38]

**Multi-stage Inert Oxidative Thermal Analysis.** To further investigate the decomposition of kerogen and the influence of oxygen, we conduct a multi-stage thermal treatment analysis, whereby we (1) dynamically heat from 40 to 600 °C at 5 °C/min in $N_2$, (2) isothermally heat at 600 °C for 30 min in $N_2$, (3) introduce air and continue isothermally heating for 30 min, and (4) dynamically heat from 600 to 1000 °C at 5 °C/min in air. TG−DSC is shown in Figure 3a, and $m/z$ = 18 and 44 are shown in Figure 3b for the multi-stage thermal analysis. The advantage in this multi-stage thermal analysis is that it allows us to highlight the thermal−chemical stabilities of kerogen and other products within the shale rock, specifically the thermal evolutions in pyrolysis versus oxidative conditions. Specific values of interest here are the total weight loss as a result of oxygen introduction, which enables us to quantify the amount of unreacted and coked kerogen, the "trapped" organics within kerogen, and $FeS_{1-x}$ species. In a $N_2$ atmosphere, brought up to 600 °C and maintained for 30 min, kerogen decomposition is complete, as seen by the flat TG curve (−4.29 wt %); all decomposition reactions evolving gaseous products have completed, and the system is in equilibrium. Below 600 °C, DSC shows an endothermic peak at 108 min (526 °C). MS supports this with $m/z$ = 18 and 44 peaks at 107 min (524 °C) and 118 min (579 °C), the combustion of oxygen and hydroxyl groups within kerogen. Once air is introduced, the unreacted and coked kerogen, the "trapped" organics within kerogen, and $Fe_{1-x}S$ species combust rapidly (−9.06 wt %), as seen by DSC and $m/z$ = 18 and 44 peaks at 159, 154, and 158 min, respectively. The evolution of $m/z$ = 64 ($SO_2$) can be seen in Figure S2 of the Supporting Information. From this analysis, we conclude that a significant portion of kerogen is left unreacted and coked during pyrolysis up to 600 °C. An iron sulfide phase, assumedly pyrrhotite, remains stable, even up to 600 °C, evidenced by the mass loss and $SO_2$ evolution.

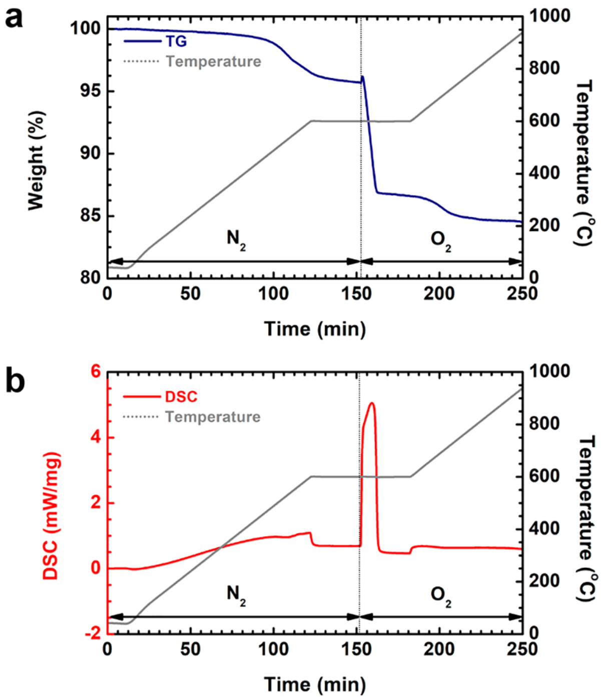

**Figure 3.** (a) TG−DSC treated in a multi-step thermal program, including changing atmospheres from nitrogen (orange) to air (blue), dynamic heating from 40 to 600 °C at 5 °C/min under nitrogen flow, isothermal heating at 600 °C for 30 min under nitrogen flow, isothermal heating for 30 min under air flow, and dynamic heating from 600 to 1000 °C at 5 °C/min under air flow. The temperature program is shown in gray. (b) Select MS of $m/z$ = 18 ($H_2O$) and $m/z$ = 44 ($CO_2$) from the multi-step thermal program.

***In Situ* DRIFTS Analysis.** The bonding specifics of shale components were investigated under thermal pyrolysis conditions *in situ* up to 600 °C and *ex situ* after isothermal pyrolysis treatment in a tube furnace at 700 and 900 °C (see panels a and b of Figure 4). Infrared peaks at low wavelengths, ∼800, ∼1000, and ∼1150 $cm^{-1}$, all correspond to Si−O bonds in silicates, such as quartz, illite, and felspar phases, present in the XRD and retained during thermal treatment.[41,42] The peaks at 714 and 879 $cm^{-1}$ suggest the presence of the calcite phase, which is also supported by the signal at ∼1450 $cm^{-1}$, the asymmetric stretching vibration of $CO_3^{2-}$.[41] *In situ*, as the temperature increases from near room temperature to 600 °C, the peak at ∼1450 $cm^{-1}$ appears to have little to no change, but *ex situ*, at 700 and 900 °C, the peak significantly decreases in intensity corresponding to the evolution of $CO_2$ as a result of calcite decomposition. This is in good agreement with our thermal analysis and *in situ* XRD data. The peaks of 1614 and ∼1680 $cm^{-1}$ correspond to the stretching vibration of C═C bonds and carbonyl C═O group bond vibrations, which can

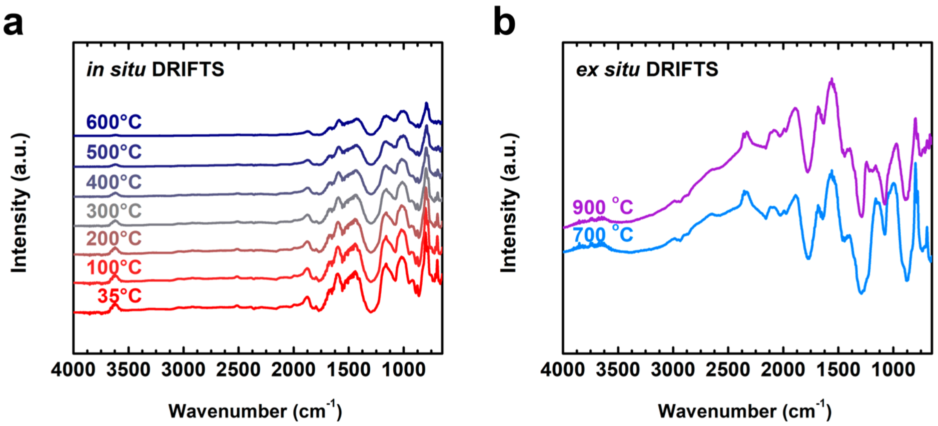

**Figure 4.** (a) *In situ* DRIFTS spectra from 30 to 600 °C in helium and (b) *ex situ* DRIFTS spectra at 30 °C following isothermal treatment at the desired temperature for 3 h in argon.

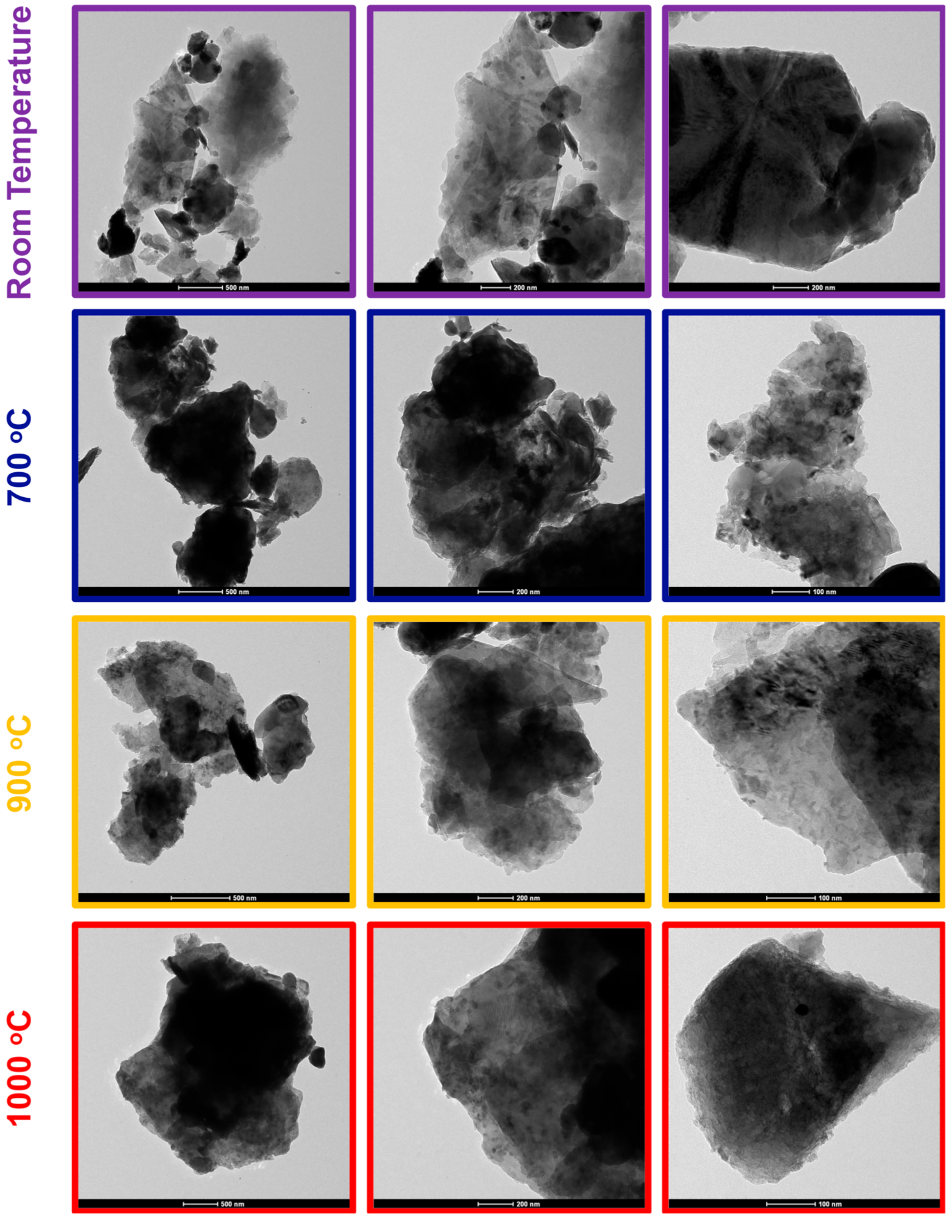

**Figure 5.** TEM of shale at room temperature and after thermal treatment in argon at 700, 900, and 1000 °C for 3 h. RT = room temperature.

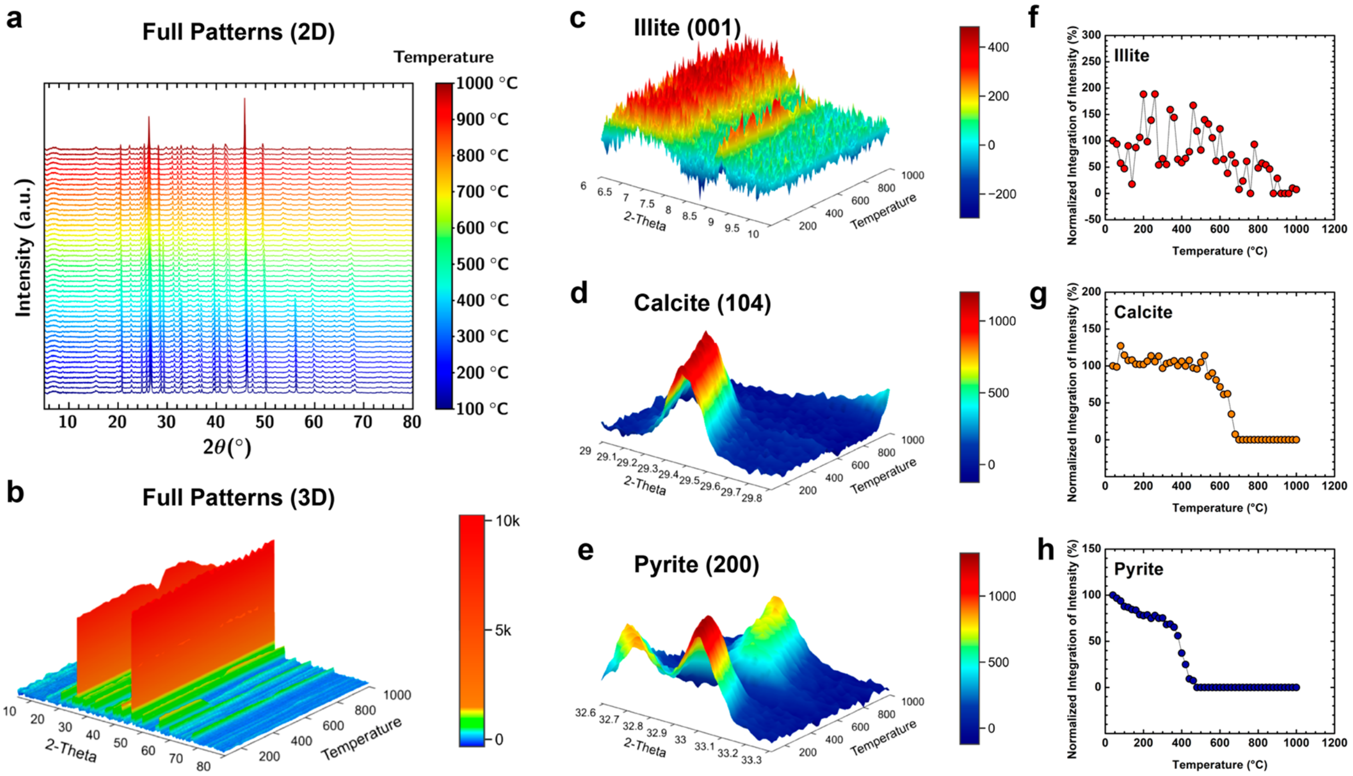

**Figure 6.** (a) 2D and (b) 3D plots of *in situ* XRD patterns, (c) 2$\theta$ of 6−10° showing the (001) peak of illite, (d) 2$\theta$ of 29−29.8° showing the (104) peak of calcite, and (e) 2$\theta$ of 32.6−33.3° showing the (200) peak of pyrite. Normalized integration of intensity from representative phase peaks (f) (001) of illite, (g) (104) of calcite, and (h) (200) of pyrite.

be associated with the complex carbon chemistry of kerogen, as seen in previous studies on the chemistry of kerogen.[41,42] *In situ*, these peaks diminish as the temperature increases to 600 °C; however, *ex situ*, the peaks remain up to even 900 °C, suggesting evidence that kerogen does not decompose completely. The pyrolysis decomposition of kerogen is significantly kinetic- and mass-transfer-limited, and the *ex situ* samples experience coking when rapidly heated to the isothermal treatment temperature, leading to the high amount of C═C and carbonyl C═O groups. In Figure S3 of the Supporting Information, the weak peaks at ∼2930 and ∼2850 $cm^{-1}$ correspond to symmetric and asymmetric stretching vibrations of $CH_2$ and $CH_3$ groups.[42] This could be from kerogen or lower weight hydrocarbons trapped within the shale. According to our data and the lack of noticeable methane or other low-weight hydrocarbons in MS, we hesitate to identify these peaks belonging to "free" hydrocarbons. As a result of the peaks at ∼2930 and ∼2850 $cm^{-1}$ vanishing above 300 °C, we assign them to free hydrocarbons as the reactions take place below what is expected from the decomposition temperature of kerogen. The peak at 3627 $cm^{-1}$ suggests isolated hydroxyl groups, which are likely to be OH surface groups of illite clay. The peak intensity of the OH stretching vibration decreases gradually with the temperature increasing from 400 to 600 °C, corresponding to the loss of the surface hydroxyl groups, as suggested by the weight loss in the TG curve and water peak in the MS curve. Hydroxyl peaks are not observed in *ex situ* samples heated to 700 and 900 °C. From this DRIFTS analysis, we draw the following conclusions that directly support our thermal analyses: the small amount of "free" hydrocarbons evolve between 100 and 400 °C; kerogen decomposes gradually with significant coking during rapid heating (10 °C/min); dehydroxylation of clays occurs between 400 and 600 °C; and most decarbonation occurs between 600 and 900 °C.

**High-Temperature Morphological Behavior.** To elucidate the morphological evolution as a result of thermal treatment, TEM was performed on samples isothermally treated in an inert atmosphere (see Figure 5). Images were taken from shale treated at room temperature and at high temperatures of 700 °C (after kerogen decomposition), 900 °C, and 1000 °C (after full carbonate decomposition). At room temperature, grains of flake-like layered clay materials and silt-sized grains of quartz, feldspar, carbonates, and pyrite are evidenced with relatively homogeneous smooth surfaces. After heat treatment to 700 °C, following partial decomposition of carbonates, pyrite, and kerogen, removal of trapped water and organic species, and dehydroxylation of clays, the morphology of each sample is quite different. The evolution and release of gases as well as decomposition of products cause cracks and crater-like openings throughout the sample. At 900 °C, only the most stable phases remain unaltered, mainly feldspar and quartz, and all carbonates are decomposed. The surfaces exhibit worm-like extrusions and large gaps, resulting from thermal decomposition and evolution of gaseous products. At 1000 °C, the extreme conditions of high-temperature treatment act to disperse the high-energy rough edges of the pores and extrusions. Clear evidence of particle growth is observed, and the sample surfaces are smoother. However, there remains large cracks, gaps, and channels, suggesting empty internal space left after decomposition of organic species. From room temperature up to 1000 °C, TEM shows large gaps of ∼10−50 nm cracks, gaps, and channels created in the minerals that remain after decomposition.

***In Situ* Mineralogical Evolutions.** The crystalline phase structure and composition were tracked during thermal treatment using *in situ* XRD up to 1000 °C. The two-dimensional (2D) full pattern plots are presented in Figure 6a, and the full range 3D plot is presented in Figure 6b. In panels c−e of Figure 6, representative peaks of major phases are presented as a function of 2$\theta$. To track the phase decomposition of each phase, we use the integrated intensity of its representative peaks, which directly suggests the total amount of the phase present. For ease of understanding, we normalized the data as a percentage of the integrated intensity of the first pattern at near-room temperature (panels f−h of Figure 6). Figure 6c shows the representative (001) peak of illite at ∼8.5°. Peak evolutions are hard to track in the pattern of illite here because of its low total intensity, which makes the changes difficult to distinguish. Additionally, the normalized integrated intensity tends to be affected by small changes in the background (see Figure 6f). However, we can still observe a general trend that illite undergoes intensity weakening beginning at above 500 °C undergoing dehydroxylation and continues until its decomposition at ∼900 °C. The decomposition of illite occurs above 500 °C when dehydroxylation begins and finishes at ∼900 °C. The decomposition of illite, a representative of clays, indicates the loss of interlayer space within the clay components of the shale.[16] This is supported by a lack of layered structures in TEM at 1000 °C (see Figure 5). In panels d and g of Figure 6, showing the representative (104) peak of calcite and its normalized integrated intensities, it is shown that calcite undergoes phase decomposition at ∼560 °C and is completely decomposed by 700 °C. Considering the kinetic limitations and mass transport from the rapid heating in TG−DSC−MS, this supports our TG−DSC−MS analysis. Calcite decomposes at above 560 °C; this pairs well with the literature.[16,37] In panels e and h of Figure 6, showing the representative (200) peak of pyrite and its normalized integrated intensities, it can be seen that pyrite undergoes intensity weakening beginning at above 100 °C as its normalized integrated intensity drops to 80% and then experiences complete decomposition from ∼300 to 460 °C. The sulfur release at ∼400 °C supports this, as shown in our thermal TG−DSC−MS analysis. In comparison to pure pyrite in an inert environment, pyrite in this shale mixture decomposes and exhibits a similar behavior at temperatures to those reported in the literature.[38] Our *in situ* XRD phase analysis supports the findings in the thermal and infrared analyses by sharing similar decomposition temperatures with synchronizing loss of representative peaks and their normalized integrated intensity.

In combination of our multi-faceted approach in investigating the thermal behavior of Marcellus shale, we are able to better understand the dynamic thermal behavior of shale. Here, we distinguish the thermal evolution of shale into three stages, as is typical when investigating non-isothermal treatment of shale.[43,44] In stage I, below 200 °C, weakly adsorbed water and other volatile species are removed. In stage II, complex kerogen decomposition occurs between 200 and 600 °C depending upon the heating rate and specific kerogen composition, mainly C/H ratio, and in stage III, above 600 °C, inorganic minerals, such as carbonate and clay materials, decompose.[19] The cracks in TEM images in Figure 5 are principally caused by carbonate, pyrite, and kerogen decomposition. Meanwhile, thermal expansion of crystalline phases and transitions of oxide components also contribute to the change in the microstructure and porosity.[45] Integrated thermal analyses and *in situ* structural and spectroscopic methodologies provide a systematic platform to deepen our understanding on the properties of shale under extreme conditions.

Pyrolysis of shale rock for the purpose of extracting hydrocarbons is a complex process as a result of the kinetic and mass transport limitations involved in the decomposition of the desired products, such as kerogen and “free” hydrocarbons, and undesired components, including water from clays, sulfur from pyrite, and carbon dioxide from carbonate. Of our highlight phases, those present in high amounts and relevant in gaseous evolutions from shale, pyrite has the lowest thermal stability, decomposing at about 400 °C, but reacts “quickly” compared to the decomposition of kerogen products, which occurs over a large range of temperatures (400−600 °C).[38] Kerogen cannot be treated as one simple compound as a result of its extremely complex carbon networks and structures formed under geochemical environments. The decomposition of kerogen is a kinetically complex phenomenon with intercompeting reactions: faster heating rates lead to higher coking, and slower heating rates lead to more evolved hydrocarbons.[34,43,46] Significant coking of kerogen occurs, evidenced especially by differences in inert/oxidative thermal analysis and multi-stage thermal analysis, which suggests significant $CO_2$ evolution directly following the introduction of oxygen at 600 °C to an inert environment. The coking of kerogen is a complex function of the heating rate and C/H ratio, which can be categorized by the origin of the organic material and age as well as kinetic and mass transport limitations.[17,20,47,48] We may have to engineer cracks and channels as observed in the morphological analysis to maximize the extraction and diffusion of organics, especially the kerogens tightly confined within the less accessible mineral structures.[6,49] The thermally induced decomposition of illite and calcite overlaps with that of kerogen as illite dehydroxylates at about 500 °C (but retains its phase structure up to ∼900 °C) and carbonate phases decompose with evolution of carbon dioxide from 550 to 900 °C. In our ongoing studies, we have expanded our investigation to link the microstructure and micromorphology with the chemical and structural evolutions under dynamic thermal conditions using a multi-scale approach employing X-ray “nano” computed tomography (nano-CT) and an in-depth crystallographic analysis.

## ■ CONCLUSION

Using analyses of contrasting multiple *in situ* techniques, we link the chemistry and microstructure of the shale with its mineralogy and thermal behavior. These insights interconnect materials science techniques to geochemical systems with pyrolysis of shale rock. The complex decomposition reactions of kerogen occurred between 200 and 600 °C depending upon the heating rate and atmosphere (oxidative or inert). During this expected range, we witnessed very little expected gaseous hydrocarbon evolution, such as methane. We anticipate this is due to exodus from pores during preparation for experiments by grinding to a fine powder. With the overlap of this key temperature range, pyrite, clay, and carbonate decomposition occurred, which prompts consideration of processing conditions and steps during the design of pyrolysis. Mirroring the escape of products evolved from organic matter and minerals at high temperatures, the remaining rock displays microscopic cracks and empty pores. Broadly, our integrated approach provides a model study for consolidating results from multiple "common" *in situ* materials science characterization techniques to investigate the complex chemistry and microstructures of natural materials.

## ASSOCIATED CONTENT

### Supporting Information

The Supporting Information is available free of charge at https://pubs.acs.org/doi/10.1021/acsearthspacechem.0c00234.

ICP−OES and LOI (Table S1), DSC−DDSC in oxygen at 5 °C/min of Marcellus shale from 600 to 1000 °C (Figure S1), MS of $m/z$ = 64 ($SO_2$) in a multi-step thermal program, including dynamic heating from 40 to 600 °C at 5 °C/min under nitrogen flow, isothermal heating at 600 °C for 30 min under nitrogen flow, isothermal heating for 30 min under air flow, and dynamic heating from 600 to 1000 °C at 5 °C/min under air flow (Figure S2), and *in situ* DRIFTS spectra from 35 to 600 °C in helium (Figure S3) (PDF)

## AUTHOR INFORMATION

### Corresponding Authors

**Hongwu Xu** − *Earth and Environmental Sciences Division, Los Alamos National Laboratory, Los Alamos, New Mexico 87545, United States*; Email: hxu@lanl.gov

**Di Wu** − *Alexandra Navrotsky Institute for Experimental Thermodynamics, The Gene and Linda Voiland School of Chemical Engineering and Bioengineering, Department of Chemistry, and Materials Science and Engineering, Washington State University, Pullman, Washington 99164, United States*; orcid.org/0000-0001-6879-321X; Email: d.wu@wsu.edu

### Authors

**Cody B. Cockreham** − *Alexandra Navrotsky Institute for Experimental Thermodynamics and The Gene and Linda Voiland School of Chemical Engineering and Bioengineering, Washington State University, Pullman, Washington 99164, United States; Earth and Environmental Sciences Division, Los Alamos National Laboratory, Los Alamos, New Mexico 87545, United States*

**Xianghui Zhang** − *Alexandra Navrotsky Institute for Experimental Thermodynamics and The Gene and Linda Voiland School of Chemical Engineering and Bioengineering, Washington State University, Pullman, Washington 99164, United States*

**Miu Lun Lau** − *Department of Computer Science, Boise State University, Boise, Idaho 83725, United States*

**Min Long** − *Department of Computer Science, Boise State University, Boise, Idaho 83725, United States; Center for Advanced Energy Studies, Idaho National Laboratory, Idaho Falls, Idaho 83415, United States*; orcid.org/0000-0001-5938-5070

**Xiaofeng Guo** − *Alexandra Navrotsky Institute for Experimental Thermodynamics, Department of Chemistry, and Materials Science and Engineering, Washington State University, Pullman, Washington 99164, United States*; orcid.org/0000-0003-3129-493X

Complete contact information is available at: https://pubs.acs.org/10.1021/acsearthspacechem.0c00234

### Notes

The authors declare no competing financial interest.

## ACKNOWLEDGMENTS

This work was supported by the institutional funds from the Gene and Linda Voiland School of Chemical Engineering and Bioengineering at Washington State University. Di Wu acknowledges the fund of Alexandra Navrotsky Institute for Experimental Thermodynamics. Cody B. Cockreham was supported by the Achievement Rewards for College Scientists (ARCS) Fellowship from the ARCS Seattle Chapter and the Natural Resource Conservation Fund (NRCEF) through the Office of Research at Washington State University. Xianghui Zhang is supported by the Chambroad Distinguished Fellowship. This work was also supported by the Department of Energy, Office of Fossil Energy, National Energy Technology Laboratory, under Grant FWP FE-406/408/409. Los Alamos National Laboratory, an affirmative action/equal opportunity employer, is operated by Triad National Security, LLC, for the National Nuclear Security Administration of the U.S. Department of Energy (Contract 89233218CNA000001).

## REFERENCES

(1) *Alternative Energy and Shale Gas Encyclopedia*; Lehr, J. H., Keeley, J., Kingery, T. B., Eds.; John Wiley & Sons, Inc.: Hoboken, NJ, 2016; DOI: 10.1002/9781119066354.

(2) *Fundamentals of Gas Shale Reservoirs*; Rezaee, R., Ed.; John Wiley & Sons, Inc.: Hoboken, NJ, 2015; DOI: 10.1002/9781119039228.

(3) Digiulio, D. C.; Jackson, R. B. Impact to Underground Sources of Drinking Water and Domestic Wells from Production Well Stimulation and Completion Practices in the Pavillion, Wyoming, Field. *Environ. Sci. Technol.* **2016**, *50* (8), 4524−4536.

(4) Nicot, J. P.; Gherabati, A.; Darvari, R.; Mickler, P. Salinity Reversal and Water Freshening in the Eagle Ford Shale, Texas, USA. *ACS Earth Sp. Chem.* **2018**, *2* (11), 1087−1094.

(5) Arthur, M. A.; Cole, D. R. Unconventional Hydrocarbon Resources: Prospects and Problems. *Elements* **2014**, *10* (4), 257−264.

(6) Bousige, C.; Ghimbeu, C. M.; Vix-Guterl, C.; Pomerantz, A. E.; Suleimenova, A.; Vaughan, G.; Garbarino, G.; Feygenson, M.; Wildgruber, C.; Ulm, F.-J.; Pellenq, R. J.-M.; Coasne, B. Realistic Molecular Model of Kerogen's Nanostructure. *Nat. Mater.* **2016**, *15*, 576−582.

(7) Yebra, M.; Quan, X.; Riaño, D.; Rozas Larraondo, P.; van Dijk, A. I. J. M.; Cary, G. J. A Fuel Moisture Content and Flammability Monitoring Methodology for Continental Australia Based on Optical Remote Sensing. *Remote Sens. Environ.* **2018**, *212*, 260−272.

(8) Xu, H. Probing Nanopore Structure and Confined Fluid Behavior in Shale Matrix: A Review on Small-Angle Neutron Scattering Studies. *Int. J. Coal Geol.* **2020**, *217*, 103325.

(9) Neil, C. W.; Hjelm, R. P.; Hawley, M. E.; Watkins, E. B.; Cockreham, C. B.; Wu, D.; Mao, Y.; Fischer, T. B.; Stokes, M. R.; Xu, H. Small-Angle Neutron Scattering (SANS) Characterization of Clay- and Carbonate-Rich Shale at Elevated Pressures. *Energy Fuels* **2020**, *34* (7), 8178−8185.

(10) Wang, Y.; Jiang, H.; Ke, Y.; Zhang, S.; Wang, L.; Wang, Y.; He, C.; Zhang, L.; Wang, J.-Q. Investigation of Pore Structures in Shallow Longmaxi Shale, South China, via Large-Area Electron Imaging and Neutron Scattering Techniques. *Energy Fuels* **2020**, *34* (7), 7974−7984.

(11) Goral, J.; Panja, P.; Deo, M.; Andrew, M.; Linden, S.; Schwarz, J.-O.; Wiegmann, A. Confinement Effect on Porosity and Permeability of Shales. *Sci. Rep.* **2020**, *10*, 49.

(12) Gao, H.; Li, H. A. Pore Structure Characterization, Permeability Evaluation and Enhanced Gas Recovery Techniques of Tight Gas Sandstones. *J. Nat. Gas Sci. Eng.* **2016**, *28*, 536−547.

(13) Ji, L.; Lin, M.; Cao, G.; Jiang, W. A Core-Scale Reconstructing Method for Shale. *Sci. Rep.* **2019**, *9*, 4364.

(14) Ma, L.; Slater, T.; Dowey, P. J.; Yue, S.; Rutter, E. H.; Taylor, K. G.; Lee, P. D. Hierarchical Integration of Porosity in Shales. *Sci. Rep.* **2018**, *8*, 11683.

(15) Liu, X.; Zhang, D. A Review of Phase Behavior Simulation of Hydrocarbons in Confined Space: Implications for Shale Oil and Shale Gas. *J. Nat. Gas Sci. Eng.* **2019**, *68*, 102901.

(16) Liu, M.; Gadikota, G. Probing the Influence of Thermally Induced Structural Changes on the Microstructural Evolution in Shale Using Multiscale X-Ray Scattering Measurements. *Energy Fuels* **2018**, *32* (8), 8193−8201.

(17) Whitelaw, P.; Uguna, C. N.; Stevens, L. A.; Meredith, W.; Snape, C. E.; Vane, C. H.; Moss-Hayes, V.; Carr, A. D. Shale Gas Reserve Evaluation by Laboratory Pyrolysis and Gas Holding Capacity Consistent with Field Data. *Nat. Commun.* **2019**, *10*, 3659.

(18) Liu, X.; Cui, P.; Ling, Q.; Zhao, Z.; Xie, R. A Review on Co-Pyrolysis of Coal and Oil Shale to Produce Coke. *Front. Chem. Sci. Eng.* **2020**, *14*, 504−512.

(19) Leenaers, A.; Van Den Berghe, S.; Koonen, E.; Kuzminov, V.; Detavernier, C. Fuel Swelling and Interaction Layer Formation in the SELENIUM Si and ZrN Coated U(Mo) Dispersion Fuel Plates Irradiated at High Power in BR2. *J. Nucl. Mater.* **2015**, *458*, 380−393.

(20) Qian, Y.; Zhan, J. H.; Lai, D.; Li, M.; Liu, X.; Xu, G. Primary Understanding of Non-Isothermal Pyrolysis Behavior for Oil Shale Kerogen Using Reactive Molecular Dynamics Simulation. *Int. J. Hydrogen Energy* **2016**, *41* (28), 12093−12100.

(21) Tiwari, P.; Deo, M. Detailed Kinetic Analysis of Oil Shale Pyrolysis TGA Data. *AIChE J.* **2012**, *58* (2), 505−515.

(22) Guo, H.; Jia, W.; Peng, P.; Zeng, J.; He, R. Evolution of Organic Matter and Nanometer-Scale Pores in an Artificially Matured Shale Undergoing Two Distinct Types of Pyrolysis: A Study of the Yanchang Shale with Type II Kerogen. *Org. Geochem.* **2017**, *105*, 56−66.

(23) Wright, A. F.; Lehmann, M. S. The Structure of Quartz at 25 and 590°C Determined by Neutron Diffraction. *J. Solid State Chem.* **1981**, *36* (3), 371−380.

(24) Tribaudino, M.; Angel, R. J.; Cámara, F.; Nestola, F.; Pasqual, D.; Margiolaki, I. Thermal Expansion of Plagioclase Feldspars. *Contrib. Mineral. Petrol.* **2010**, *160*, 899−908.

(25) Eppelbaum, L.; Kutasov, I.; Pilchin, A. Thermal Properties of Rocks and Density of Fluids. *Lect. Notes Earth Syst. Sci.* **2014**, 99−149.

(26) Beruto, D. T.; Searcy, A. W.; Kim, M. G. Microstructure, Kinetic, Structure, Thermodynamic Analysis for Calcite Decomposition: Free-Surface and Powder Bed Experiments. *Thermochim. Acta* **2004**, *424* (1−2), 99−109.

(27) Lambert, J. M.; Simkovich, G.; Walker, P. L. Kinetics and Mechanism of the Pyrite-to-Pyrrhotite Transformation. *Metall. Mater. Trans. B* **1998**, *29*, 385−396.

(28) Sharma, S.; Carr, T. R.; Mouser, P. J.; Wrighton, K.; Wilkins, M.; Darrah, T.; Hakala, A. Biogeochemical Characterization of Core, Fluids, and Gas at MSEEL Site. *Proceedings of the SPE/AAPG/SEG Unconventional Resources Technology Conference*; Austin, TX, July 24−26, 2017; DOI: 10.15530/urtec-2017-2669965.

(29) Zhang, X.; Cockreham, C. B.; Huang, Z.; Sun, H.; Yang, C.; Marin-Flores, O. G.; Wang, B.; Guo, X.; Ha, S.; Xu, H.; Wu, D. Thermodynamics of Water−Cationic Species-Framework Guest−Host Interactions within Transition Metal Ion-Exchanged Mordenite Relevant to Selective Anaerobic Oxidation of Methane to Methanol. *J. Phys. Chem. Lett.* **2020**, *11* (12), 4774−4784.

(30) Zhang, X.; Cockreham, C. B.; Yılmaz, E.; Li, G.; Li, N.; Ha, S.; Fu, L.; Qi, J.; Xu, H.; Wu, D. Energetic Cost for Being "Redox-Site-Rich" in Pseudocapacitive Energy Storage with Nickel−Aluminum Layered Double Hydroxide Materials. *J. Phys. Chem. Lett.* **2020**, *11* (9), 3745−3753.

(31) Li, G.; Zhang, X.; Qiu, D.; Liu, Z.; Yang, C.; Cockreham, C. B.; Wang, B.; Fu, L.; Zhang, J.; Sudduth, B.; Guo, X.; Sun, H.; Huang, Z.; Qi, J.; Sun, J.; Ha, S.; Wang, Y.; Wu, D. Tuning Ni/Al Ratio to Enhance Pseudocapacitive Charge Storage Properties of Nickel−Aluminum Layered Double Hydroxide. *Adv. Electron. Mater.* **2019**, *5* (8), 1900215.

(32) Cockreham, C.; Zhang, X.; Li, H.; Hammond-Pereira, E.; Sun, J.; Saunders, S. R.; Wang, Y.; Xu, H.; Wu, D. Inhibition of $AlF_3{\cdot}3H_2O$ Impurity Formation in $Ti_3C_2T_x$ MXene Synthesis under a Unique $CoF_x$/HCl Etching Environment. *ACS Appl. Energy Mater.* **2019**, *2* (11), 8145−8152.

(33) Schneider, C. A.; Rasband, W. S.; Eliceiri, K. W. NIH Image to ImageJ: 25 Years of Image Analysis. *Nat. Methods* **2012**, *9*, 671−675.

(34) Tiwari, P.; Deo, M. Compositional and Kinetic Analysis of Oil Shale Pyrolysis Using TGA-MS. *Fuel* **2012**, *94*, 333−341.

(35) L'vov, B. V. Mechanism of Thermal Decomposition of Alkaline-Earth Carbonates. *Thermochim. Acta* **1997**, *303* (2), 161−170.

(36) L'Vov, B. V. Mechanism and Kinetics of Thermal Decomposition of Carbonates. *Thermochim. Acta* **2002**, *386* (1), 1−16.

(37) Radha, A. V.; Fernandez-Martinez, A.; Hu, Y.; Jun, Y. S.; Waychunas, G. A.; Navrotsky, A. Energetic and Structural Studies of Amorphous $Ca_{1-x}Mg_xCO_3{\cdot}nH_2O$ ($0 \le x \le 1$). *Geochim. Cosmochim. Acta* **2012**, *90*, 83−95.

(38) Xu, H.; Guo, X.; Seaman, L. A.; Harrison, A. J.; Obrey, S. J.; Page, K. Thermal Desulfurization of Pyrite: An in Situ High-T Neutron Diffraction and DTA-TGA Study. *J. Mater. Res.* **2019**, *34* (19), 3243−3253.

(39) Ropp, R. C. Encyclopedia of the Alkaline Earth Compounds. *Choice Rev. Online* **2014**, *51* (7), 51-3588.

(40) Hu, G.; Dam-Johansen, K.; Wedel, S.; Hansen, J. P. Decomposition and Oxidation of Pyrite. *Prog. Energy Combust. Sci.* **2006**, *32* (3), 295−314.

(41) Gasaway, C.; Mastalerz, M.; Krause, F.; Clarkson, C.; Debuhr, C. Applicability of Micro-FTIR in Detecting Shale Heterogeneity. *J. Microsc.* **2017**, *265* (1), 60−72.

(42) Washburn, K. E.; Birdwell, J. E. Multivariate Analysis of ATR-FTIR Spectra for Assessment of Oil Shale Organic Geochemical Properties. *Org. Geochem.* **2013**, *63*, 1−7.

(43) Liu, Q. Q.; Han, X. X.; Li, Q. Y.; Huang, Y. R.; Jiang, X. M. TG-DSC Analysis of Pyrolysis Process of Two Chinese Oil Shales. *J. Therm. Anal. Calorim.* **2014**, *116*, 511−517.

(44) Jiang, X. M.; Han, X. X.; Cui, Z. G. Mechanism and Mathematical Model of Huadian Oil Shale Pyrolysis. *J. Therm. Anal. Calorim.* **2006**, *86*, 457−462.

(45) Shen, Y.-J.; Zhang, Y.-L.; Gao, F.; Yang, G.-S.; Lai, X.-P. Influence of Temperature on the Microstructure Deterioration of Sandstone. *Energies* **2018**, *11* (7), 1753.

(46) Bai, F.; Guo, W.; Lü, X.; Liu, Y.; Guo, M.; Li, Q.; Sun, Y. Kinetic Study on the Pyrolysis Behavior of Huadian Oil Shale via Non-Isothermal Thermogravimetric Data. *Fuel* **2015**, *146*, 111−118.

(47) Tiwari, P. Oil Shale Pyrolysis: Benchscale Experimental Studies and Modeling. Ph.D. Thesis, Department of Chemical Engineering, The University of Utah, Salt Lake City, UT, 2012.

(48) Zhao, X.; Zhang, X.; Liu, Z.; Lu, Z.; Liu, Q. Organic Matter in Yilan Oil Shale: Characterization and Pyrolysis with or without Inorganic Minerals. *Energy Fuels* **2017**, *31* (4), 3784−3792.

(49) Chen, J.; Xiao, X. Evolution of Nanoporosity in Organic-Rich Shales during Thermal Maturation. *Fuel* **2014**, *129*, 173−181.

## ■ NOTE ADDED AFTER ASAP PUBLICATION

This paper was originally published ASAP on November 30, 2020. A correction was made the the Figure 2f caption, and the paper was reposted on December 8, 2020.